

Surrogate-assisted airfoil optimization in rarefied gas flows

Xiaoda Li, Ruifeng Yuan, Yanbing Zhang, Lei Wu*

*Department of Mechanics and Aerospace Engineering, Southern University of Science and Technology,
Shenzhen 518055, China*

Abstract

With growing interest in space exploration, optimized airfoil design has become increasingly important. However, airfoil design in rarefied gas flows remains underexplored because solving the Boltzmann equation formulated in a six-dimensional phase space is time-consuming. To address this problem, a solver-in-the-loop Bayesian optimization framework for symmetric, thickness-only airfoils is developed. First, airfoils are parameterized using a class-shape transformation that enforces geometric admissibility. Second, a Gaussian-process expected-improvement surrogate is coupled in batches to a fast-converging, asymptotic-preserving Boltzmann solver for sample-efficient exploration. Drag-minimizing airfoils are identified in a wide range of gas rarefaction. It is found that, at Mach numbers $M_\infty = 2$ and 4, the streamwise force increases with the gas rarefaction and shifts from pressure-dominated to shear-dominated drag, while optimization reduces drag at all conditions. The benefit of optimization peaks in the weakly rarefied regime—about 30% at $M_\infty = 2$ and 40 ~ 50% at $M_\infty = 4$ —and falls to a few percent in transition and free-molecular flow regimes. Drag decomposition shows that these gains come mainly from reduced pressure drag, with viscous drag almost unchanged. The optimal airfoils form a coherent rarefaction-aware family: they retain a smooth, single-peaked thickness profile, are aft-loaded at low gas rarefaction, and exhibit a forward shift of maximum thickness and thickness area toward mid-chord as gas rarefaction increases. These trends provide a physically interpretable map that narrows the design space.

Keywords: Rarefied gas dynamics, airfoil optimization, Bayesian optimization

1. Introduction

Shape optimization plays a crucial role in space exploration and high-speed aerospace applications, where vehicle performance, thermal protection, and fuel efficiency are strongly influenced by aerodynamic design. In many regimes encountered during high-altitude flight and atmospheric reentry, the Knudsen number (Kn, defined as the ratio of molecular mean free path to characteristic flow length) becomes appreciable, and the Navier–Stokes (NS)

*Corresponding authors:

Email address: wul@sustech.edu.cn (Lei Wu)

equations break down [1]. In these conditions, a kinetic description based on the Boltzmann equation or its model formulations is required to capture the rarefied gas dynamics, which is quite different to continuum gas dynamics. For example, numerical studies show that increasing Kn systematically alters lift-to-drag ratio and flow structure [2, 3]. However, solving the Boltzmann equation is computationally challenging due to its high dimensionality in phase space, which severely limits the feasibility of routine simulations for design and optimization. As a result, despite its critical importance for the design of spacecraft and hypersonic vehicles [4, 5], shape optimization in rarefied gas flows remains less developed than in continuum aerodynamics.

Shape optimization approaches can be grouped into two lines: gradient-based local search that relies on sensitivities, and surrogate-model strategies that use a limited number of high-fidelity samples. In the first line, an adjoint system for the chosen flow model is derived and the resulting gradients are used to update high-dimensional design variables efficiently. For continuum flows, gradient-based optimization based on the Navier–Stokes equations has become a standard tool for aerodynamic shape design, where adjoint methods provide gradients of the objective function at a computational cost that is independent of the number of design variables, enabling efficient optimization of wings and airfoils with many design parameters [6–8]. For rarefied gas flows, adjoint topology-optimization formulations have recently been constructed for Boltzmann kinetic equations and applied to rarefied microdevices and channels [9–12]. These kinetic adjoint approaches, however, require elaborate derivations and intrusive code changes, since boundary conditions and multiscale couplings are algebraically complex and substantial changes in operating conditions or kinetic models often trigger further implementation effort.

In the second line, the mapping from geometry to objective is treated as a black-box function and a surrogate is built on a finite set of training samples to guide subsequent evaluations. Common choices include radial-basis-function interpolants, Gaussian-process models, and neural-network regressors, combined with acquisition rules such as expected improvement, probability of improvement, and upper confidence bounds or related local–global trade-off mechanisms [13–17]. Compared with gradient-based methods, these strategies do not require analytic sensitivities, are more robust to non-smooth or noisy objectives, and can be wrapped around different flow solvers without modifying their internal implementation. Their performance, however, is constrained by the number and placement of expensive kinetic evaluations: when each sample demands a high-fidelity solver of the Boltzmann equation [18–20] and the design space has moderate dimension, only a small number of evaluations is affordable and standard surrogate schemes struggle to reconcile global search with local convergence. In addition, if the shape parameterization is not properly regularized, the search tends to generate highly oscillatory airfoils that are difficult to mesh or manufacture [21, 22]. These limitations naturally raise the question: can the shape space, surrogate model, and sampling strategy be designed in a coordinated way so that, without sacrificing the fidelity of kinetic evaluations and under a limited evaluation budget, the optimal airfoil shapes corresponding to a broad range of Knudsen numbers can be identified?

To address this question, we develop a Bayesian optimization framework for symmetric, thickness-only airfoils in rarefied supersonic flow. We parameterize airfoils using a

class-shape transformation (CST) with eight design variables and restrict them to a geometrically admissible set that enforces symmetry, smoothness, and basic thickness and area constraints [21–24]. Over this regularized shape space, we construct a Gaussian-process surrogate with batched expected-improvement acquisition and incorporate simple feasibility and locality controls [13–17]. We couple the surrogate in a solver-in-the-loop framework to an efficient kinetic Boltzmann solver [25–27], which provides variance-free evaluations of the dimensionless streamwise force. This approach enables sample-efficient exploration of rarefied airfoil designs and allows us to identify drag-minimizing airfoils from slip to transition and toward the free-molecular flow regime.

The remainder of the paper is organized as follows: Section 2 formulates the optimization problem, introduces the CST-based airfoil parameterization and geometric admissible set, and summarizes the mesh generation and kinetic-solver setup. Section 3 presents the surrogate-based optimization methodology. Section 4 reports the shape optimization results of the supersonic airfoil over a wide range of Knudsen numbers. Section 5 concludes and outlines directions for future work.

2. Problem formulation and numerical setup

In this section, the airfoil optimization problem is formulated, the CST parameterization and admissible geometries are described, and the mesh generation procedure and multiscale kinetic solver are presented.

2.1. Objective definition

Given the airfoil geometry and operating condition (i.e., the Mach number M_∞ and Knudsen number Kn), the wall pressure p_w and viscous shear-stress tensor $\boldsymbol{\tau}_w$ on all wall faces can be obtained by solving the Boltzmann kinetic equation. From these fields, the dimensionless streamwise force per unit span, denoted by D , is then constructed and used as the objective in the subsequent shape optimization.

The total wall stress $\boldsymbol{\sigma}_w$ and the traction vector \mathbf{t} on the wall are

$$\boldsymbol{\sigma}_w = p_w \mathbf{I} + \boldsymbol{\tau}_w, \quad \mathbf{t} = \boldsymbol{\sigma}_w \cdot \mathbf{n}, \quad (1)$$

where \mathbf{n} is the outward unit normal pointing into the solid. Using the free-stream direction $\hat{\mathbf{e}}_x = (1, 0)$ as the projection axis, the non-dimensional streamwise force per unit span is defined as

$$D = -\frac{1}{p_\infty c} \int_{\partial\Omega_w} \mathbf{t} \cdot \hat{\mathbf{e}}_x \, ds, \quad (2)$$

where $p_\infty = \frac{1}{2}\rho_\infty U_\infty^2$ is the free-stream dynamic pressure and c is the chord length. The minus sign enforces an upwind-positive convention so that $D > 0$ corresponds to drag along the incoming flow.

For non-dimensional geometries we take $c = 1$. We are going to minimize the drag force at the given set (M_∞, Kn) , when the area of airfoil is no larger than that of the canonical NACA0012 airfoil.

2.2. CST-based airfoil parameterization and geometric admissibility

To minimize the objective D over a tractable design space, the airfoil geometry is represented using the CST formulation. At the same time, the design space is simplified by restricting attention to symmetric, thickness-only airfoils, so that the CST formulation can be simplified accordingly.

Let $x \in [0, 1]$ denote the chordwise coordinate from the leading edge ($x = 0$) to the trailing edge ($x = 1$). The upper and lower surfaces of the airfoil can be described as

$$y_u(x) = \frac{1}{2}t(x), \quad y_\ell(x) = -\frac{1}{2}t(x), \quad (3)$$

where

$$t(x) = 2x^{N_1}(1-x)^{N_2} \sum_{k=0}^5 A_k B_k^{(5)}(x), \quad (4)$$

with $B_k^{(m)}(x) = \binom{m}{k} x^k (1-x)^{m-k}$ being the Bernstein polynomials and $\{A_k\}_{k=0}^5$ the Bernstein coefficients. Here, N_1 and N_2 are positive, and the sharpness or bluntness of the leading and trailing edges is controlled by N_1 and N_2 , respectively. Each candidate section is therefore fully determined by the six coefficients $\{A_k\}$ and the two class-function exponents (N_1, N_2) , which form the design vector used throughout the optimization:

$$\boldsymbol{\theta} = (A_0, A_1, A_2, A_3, A_4, A_5, N_1, N_2) \in \mathbb{R}^8. \quad (5)$$

To keep the designs within a physically reasonable region, the design variables are first restricted to a simple box in parameter space. In particular, the thickness coefficients A_0, \dots, A_5 are required to lie in the range of $[0.02, 0.22]$, and the class-function exponents N_1 and N_2 are confined to the range of $[0.01, 2.00]$. These bounds are chosen empirically so that the resulting sections bracket the baseline NACA0012 thickness while excluding needle-like geometries and overly blunt leading or trailing edges. These bounds serve as the global parameter ranges for all optimization runs.

To exclude pathological shapes before meshing and flow simulation, the design vector is further restricted to a geometrically admissible set. All checks are performed on a fixed chordwise grid $\{x_i\}_{i=0}^n \subset [0, 1]$. First, non-intersection of the upper and lower surfaces can be enforced naturally by imposing the constraint $A_k > 0$. Second, the thickness is required to be unimodal. Denoting the maximum thickness and the peak position by $x_{t,\max} = \arg \max t(x)$ and $t_{\max} = t(x_{t,\max})$, respectively, the following constraints are applied:

$$\begin{cases} \frac{dt}{dx} > 0, & \text{for } x < x_{t,\max}, \\ \frac{dt}{dx} < 0, & \text{for } x > x_{t,\max}, \end{cases} \quad (6)$$

Third, to limit excessive curvature and small-scale waviness, the curvature of both surfaces is constrained to change sign at most twice along the chord. Finally, global thickness measures are constrained to avoid needle-like or excessively thick sections. The sectional area

$\int_0^1 t(x)dx$ is required to exceed a prescribed minimum area (taken as the area of the canonical NACA0012 in the present non-dimensionalization), and the peak thickness and its location satisfy

$$\frac{t_{\max}}{c} < 0.25, \quad \frac{x_{t,\max}}{c} \in [0.2, 0.8]. \quad (7)$$

The geometrically admissible set \mathcal{A} thus consists of all design vectors $\boldsymbol{\theta}$ that lie within the parameter ranges and for which the corresponding surfaces (3) satisfy above constraints. This construction removes nonphysical or numerically fragile shapes while retaining sufficient flexibility for meaningful aerodynamic variations.

2.3. Mesh generation

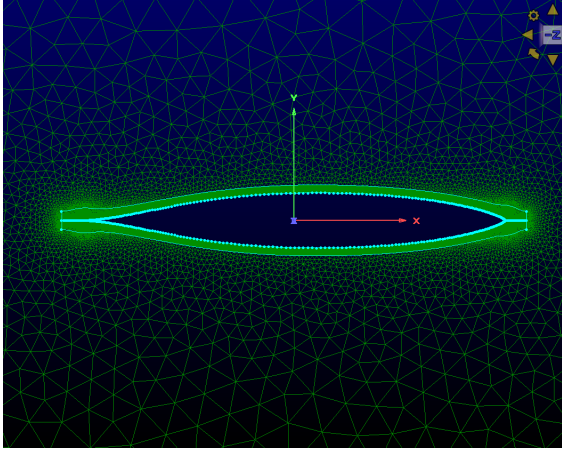
Since the CST parameters are allowed to vary over a broad range, the generated airfoils can become extremely sharp at the leading and trailing edges, which tends to generate nearly degenerate grid cells and, in some cases, even causes failure of the high-fidelity flow solver. Besides, within our sample-intensive optimization workflow, where hundreds of candidate designs must be evaluated one by one, manually adjusting the mesh for each case is infeasible in both time and labor. Therefore, a scripted workflow is designed in the commercial mesh generator Pointwise that automatically identifies the endpoint geometry of each airfoil and selects the corresponding meshing procedure.

The endpoint geometry is inferred from the CST exponents N_1 and N_2 : if N_1 (or N_2) > 0.65 the leading (or trailing) edge is classified as sharp and otherwise as blunt. Based on this classification, one of four scripts is selected: **ss** (sharp leading edge, sharp trailing edge), **sb** (sharp leading edge, blunt trailing edge), **bs** (blunt leading edge, sharp trailing edge), and **bb** (blunt leading edge, blunt trailing edge).

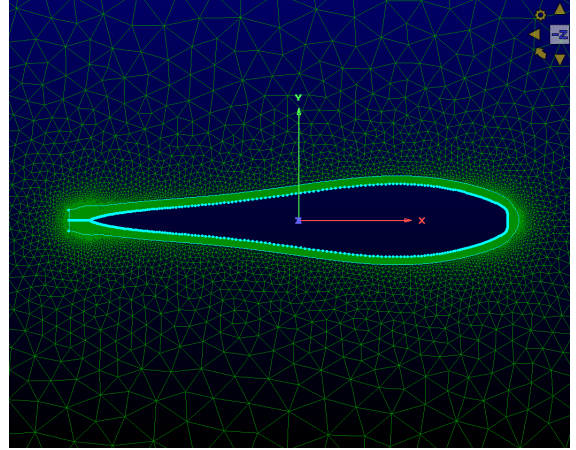
These four scripts differ in two aspects. On the one hand, for any sharp endpoint, a short tangential cap is added to close the upper and lower surfaces and to provide a well-shaped edge for extrusion; for a blunt endpoint, the CST-generated finite-thickness nose or tail is used directly as the wall boundary. On the other hand, for **bb**, **bs** and **sb** cases, the upper and lower surfaces (including any nose cap) form a single closed boundary that is extruded as one ring. For sharp–sharp (**ss**) cases, the two sides are instead extruded as separate bands to reduce distortion near sharp trailing edges.

The upper and lower surfaces are reparameterized by arc length and sampled with 201 nodes per side, with endpoint spacings of $0.0008c$ near the nose and tail. This yields nearly uniform sampling and a stable inner curve for the body-fitted strip. The same normal-extrusion parameters are used in all cases: first-layer thickness $5 \times 10^{-4}c$, growth factor 1.04, and 25 layers, followed by a light smoothing. During this step, the innermost ring is kept fixed and serves as a geometric reference, so that edge ordering, normals, and segment lengths remain consistent with the drag integral in Section 2.1. Typical meshes are shown in Fig. 1.

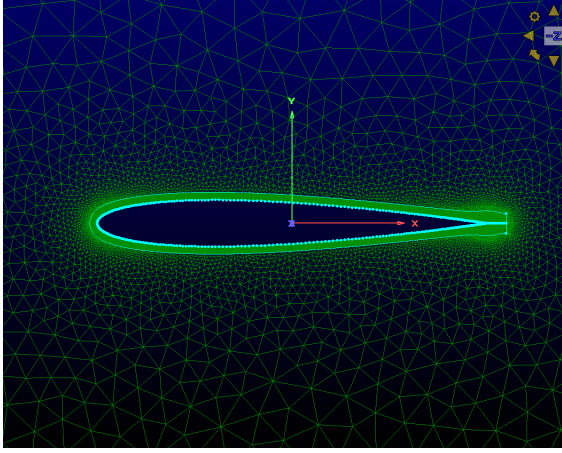
The far field is a circle of radius $10c$ centered at the airfoil centroid and discretized with 40 nodes. Together with the outer edge of the body-fitted strip, it forms an annular region that is filled with an unstructured mesh. Because the airfoil shape varies between cases, the



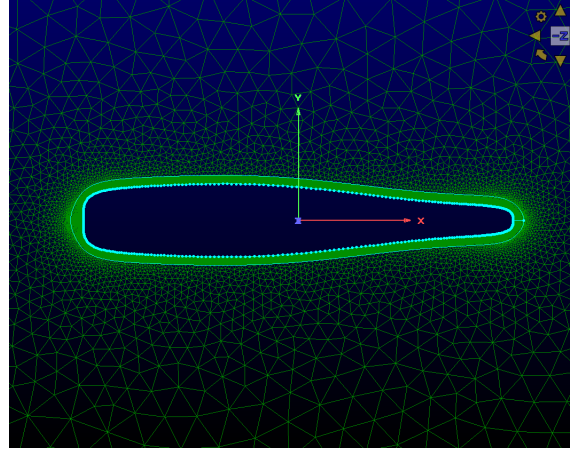
(a) sharp leading edge, sharp trailing edge



(b) sharp leading edge, blunt trailing edge



(c) blunt leading edge, sharp trailing edge



(d) blunt leading edge, blunt trailing edge

Figure 1: Representative meshes for the four endpoint topologies.

total number of cells also changes; nevertheless, each grid file contains approximately 20,000 cells. In the grid files, the airfoil surface and outer circle are tagged as wall and far field boundaries, where the diffuse and Maxwellian equilibrium boundary conditions are applied, respectively [27].

2.4. Deterministic kinetic solver

While every geometrically admissible design vector $\boldsymbol{\theta} \in \mathcal{A}$ in Section 2.2 is mapped automatically to a CFD-ready mesh, a high-fidelity flow solver is needed to calculate the rarefied gas dynamics. When the Knudsen number becomes appreciable, the NS equations become inaccurate and the gas flow has to be described at the kinetic level.

Consider a polyatomic gas with d internal degrees of freedom. Two reduced velocity distribution functions, $f_0(\mathbf{x}, \mathbf{v})$ and $f_1(\mathbf{x}, \mathbf{v})$, are introduced to describe the translational and internal states of the gas, respectively, where $\mathbf{x} = (x, y, z)$ is the spatial coordinate and $\mathbf{v} = (v_x, v_y, v_z)$ is the molecular velocity. Denoting the density by ρ , the flow velocity by \mathbf{u} ,

the traceless stress tensor by $\boldsymbol{\sigma}$, the translational and internal temperatures by T_t and T_r , and the corresponding heat fluxes by \mathbf{q}_t and \mathbf{q}_r , one has

$$\begin{aligned} (\rho, \rho\mathbf{u}, \boldsymbol{\sigma}, \tfrac{3}{2}\rho RT_t, \mathbf{q}_t) &= \int_{\mathbb{R}^3} (1, \mathbf{v}, \mathbf{c}\mathbf{c} - \tfrac{c^2}{3}\mathbf{I}, \tfrac{c^2}{2}, \tfrac{c^2}{2}\mathbf{c}) f_0 d\mathbf{v}, \\ (\tfrac{d}{2}\rho RT_r, \mathbf{q}_r) &= \int_{\mathbb{R}^3} (1, \mathbf{c}) f_1 d\mathbf{v}, \end{aligned} \quad (8)$$

where $\mathbf{c} = \mathbf{v} - \mathbf{u}$ is the peculiar velocity, \mathbf{I} is the 3×3 identity tensor, and R is the gas constant. The translational pressure is $p_t = \rho RT_t$, while the total temperature $T = (3T_t + dT_r)/(3 + d)$ defines the equilibrium temperature between translational and internal modes, with total pressure $p = \rho RT$.

The evolution of the reduced VDFs is governed by the modified Rykov model [28, 29], which in the present steady-state problems takes the form

$$\mathbf{v} \cdot \nabla_{\mathbf{x}} f_i = \frac{g_{i,t} - f_i}{\tau} + \frac{g_{i,r} - g_{i,t}}{Z_r \tau}, \quad i = 0, 1, \quad (9)$$

where $g_{i,t}$ and $g_{i,r}$ are reference (translational and internal) equilibrium distributions, $Z_r = 2.667$ is the internal collision number that controls the relaxation of internal energy toward translational equilibrium, and τ is the mean collision time of gas molecules. The specific forms of $g_{0,t}$, $g_{0,r}$, $g_{1,t}$ and $g_{1,r}$ are chosen such that the model reproduces the correct shear viscosity and thermal conductivity for diatomic gases, see Refs. [29, 30] for details.

The collision time is related to the local shear viscosity and pressure through

$$\tau = \frac{\mu(T_t)}{p_t}, \quad \mu(T_t) = \mu(T_0) \left(\frac{T_t}{T_0} \right)^\omega, \quad (10)$$

where $\mu(T_t)$ is the gas viscosity, T_0 is a reference temperature, and ω is the viscosity index associated with the intermolecular potential; in this paper, we choose $\omega = 0.75$ for nitrogen gas, with $d = 2$. The Knudsen number is defined at the reference pressure p_0 and temperature T_0 as

$$\text{Kn} = \frac{\mu(T_0)}{p_0 L} \sqrt{\frac{\pi R T_0}{2}}. \quad (11)$$

The kinetic model above is formulated with three translational degrees of freedom, but in the numerical implementation we restrict attention to planar flows and assume that the distribution function is independent of the out-of-plane velocity component. As a result, the three-dimensional velocity integrals reduce to integrals over the in-plane components (v_x, v_y) and are evaluated on a truncated two-dimensional velocity domain $(v_x, v_y) \in [-V_{x,\max}, V_{x,\max}] \times [-V_{y,\max}, V_{y,\max}]$, and discretized by a uniform Cartesian grid with $N_{v_x} \times N_{v_y}$ nodes. Specifically, we use

$$\begin{aligned} (V_{x,\max}, V_{y,\max}, N_{v_x}, N_{v_y}) &= (10, 8, 50, 40) \quad \text{for } M_\infty = 2, \\ (V_{x,\max}, V_{y,\max}, N_{v_x}, N_{v_y}) &= (14, 12, 70, 60) \quad \text{for } M_\infty = 4. \end{aligned} \quad (12)$$

For each Mach number, this velocity grid is kept fixed over all Knudsen numbers considered, and velocity moments such as density, stress, and heat flux are approximated by simple quadrature over the corresponding discrete velocity set [27].

Since conventional discrete-velocity methods tend to converge slowly when the flow approaches the near-continuum regime, the general synthetic iterative scheme (GSIS) [25–27] is adopted to accelerate convergence. GSIS is built on a discrete-velocity, finite-volume discretization of Eq. (9), but augments it with a synthetic macroscopic system rigorously derived from the kinetic equation. That is, at each iteration, macroscopic moments $\mathbf{W} = (\rho, \mathbf{u}, T)$, representing the conservative densities of mass, momentum, and total energy, are first evaluated from the current kinetic solution. An auxiliary macroscopic system is then solved to obtain an updated field \mathbf{W} that is asymptotically consistent with the NS equations in the small-Kn limit. This updated macroscopic field is fed back to precondition and constrain the kinetic update, yielding new velocity distribution functions f_0 and f_1 . The process is repeated until both f and \mathbf{W} converge. This synthetic macro-meso coupling enables fast-converging, asymptotic-preserving simulations of rarefied gas flows, typically reaching steady state within a few dozen iterations while allowing spatial cell sizes much larger than the molecular mean free path. As a consequence, a steady GSIS solve for a single airfoil at one operating condition (M_∞, Kn) typically requires about $2 \sim 3$ minutes of wall-clock time for $M_\infty = 2$ when run on 60 cores [27].

An isothermal diffuse-reflection boundary condition is imposed at the solid wall [26], where the wall temperature equals that of the incoming flow at far field. To evaluate the drag objective, the stresses acting on the airfoil surface are obtained from the kinetic solution at the solid wall. Since GSIS is deterministic and variance-free, quantities such as drag remain stable across iterations and designs, which is crucial for robust comparison in optimization.

3. Surrogate Optimization

The solver-in-the-loop workflow to minimize the drag is shown in Fig. 2. The loop is built around a Gaussian-process surrogate with automatic relevance determination (ARD) [13] in Section 3.1, which is initially trained on 40 admissible airfoil designs generated by Latin hypercube sampling [31] and evaluated by GSIS. In each of 50 subsequent optimization rounds, an expected improvement (EI) acquisition rule [14] is used to score candidate designs, and a batch of four new designs is selected for high-fidelity GSIS evaluation and appended to the training set (Section 3.2). To improve robustness and accelerate convergence under this limited evaluation budget, the feasibility-aware filters, box-based locality controls, and simple parameter-tuning strategies that modify the candidate generation, scoring, and batch-selection, is introduced in Section 3.3. The choices of 40 initial designs and 50 optimization rounds are based on empirical tests that balance surrogate accuracy against overall computational cost.

3.1. Gaussian-process with ARD

For a fixed operating condition (M_∞, Kn) , the design vector introduced in Section 2.2 is denoted by $\boldsymbol{\theta} \in \mathcal{A}$ and is represented here by the raw input vector $\tilde{\mathbf{x}} \in \mathbb{R}^8$, i.e. $\tilde{\mathbf{x}} \equiv \boldsymbol{\theta}$. The corresponding target is the steady drag $\tilde{y} = D(\boldsymbol{\theta}; M_\infty, \text{Kn})$.

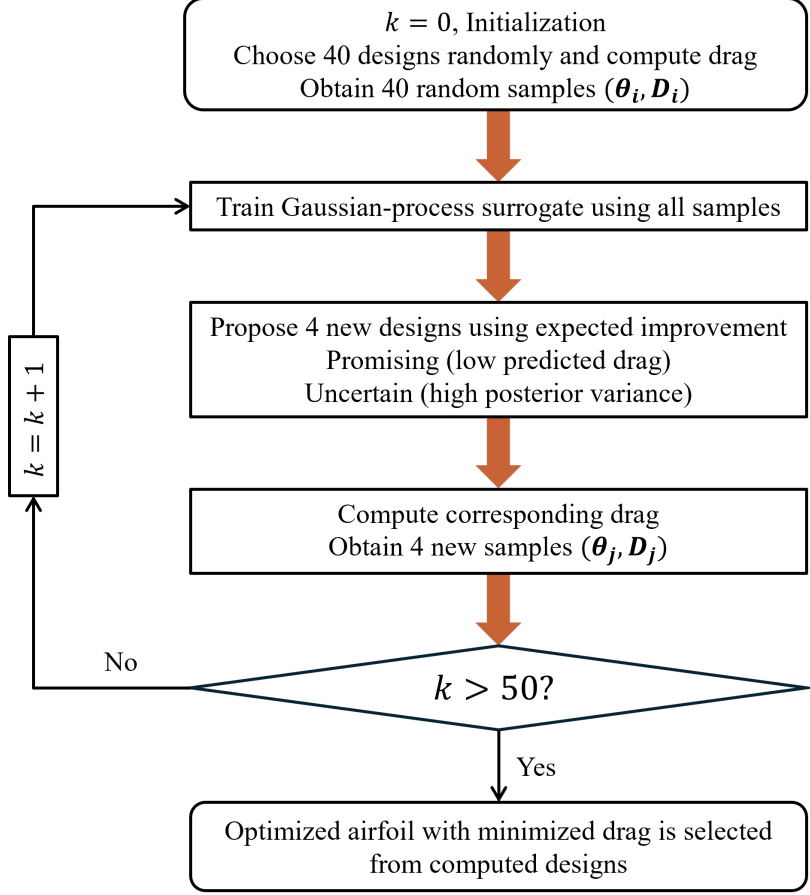


Figure 2: Surrogate-assisted optimization workflow at a fixed operating condition (M_∞, Kn) .

For the design variables, it is convenient to apply a simple normalization so that all components share a comparable scale and the minimum distance filters and trust region updates can be formulated in a common coordinate system. Let lo_j and hi_j be the componentwise minima and maxima of the raw inputs over the current training set. Each component is then mapped to a normalized coordinate by $x_j = (\tilde{x}_j - \text{lo}_j) / (\max(\text{hi}_j - \text{lo}_j, 10^{-6}))$, where a lower bound of 10^{-6} is added to avoid division by very small numbers.

The scalar outputs are treated differently. To improve the numerical conditioning of the Gaussian-process regression and to match a zero-mean prior, the raw responses \tilde{y} are standardized rather than merely rescaled. Specifically, the standardized output is defined as $y = (\tilde{y} - \bar{y}) / s_y$, where \bar{y} and s_y are the sample mean and standard deviation of the raw outputs. With this treatment, y has approximately zero mean and unit variance and is well conditioned for hyperparameter estimation.

On the normalized design space, let $y(\mathbf{x})$ denote the standardized drag response at input \mathbf{x} . A Gaussian-process prior is placed on this scalar response,

$$y(\cdot) \sim \mathcal{GP}(0, k_\eta(\cdot, \cdot)), \quad (13)$$

where the first argument 0 is the prior mean function, chosen to be identically zero because

the standardized outputs have approximately zero mean. The covariance kernel k_η encodes similarity and smoothness. To allow different sensitivities along different CST parameters, a Matérn-5/2 kernel with automatic relevance determination (ARD) is used [13]:

$$k_\eta(\mathbf{x}, \mathbf{x}') = \sigma^2 \left(1 + \sqrt{5} r + \frac{5}{3} r^2 \right) \exp(-\sqrt{5} r), \quad (14)$$

where $r(\mathbf{x}, \mathbf{x}') = \sqrt{\sum_{j=1}^8 (x_j - x'_j)^2 / \ell_j^2}$ is the scaled Euclidean distance in the normalized design space. Here the ℓ_j are ARD length scales that control the sensitivity of the response to the j -th CST parameter: smaller ℓ_j permit more rapid variation along that direction, while larger ℓ_j correspond to weaker dependence. The parameter σ^2 is the process variance that sets the overall magnitude of the function variations. In the implementation, all length scales are initialized to $\ell_j = 1$ and the process variance is initialized to $\sigma^2 = 1$, with bounds $\ell_j \in [10^{-3}, 10^5]$ and $\sigma^2 \in [10^{-4}, 10^4]$. These quantities are treated as hyperparameters of the surrogate model and will be learned and updated from the training data as the optimization proceeds.

Given the training data $X = [\mathbf{x}_1, \dots, \mathbf{x}_n]^\top$ and $\mathbf{y} = [y(\mathbf{x}_1), \dots, y(\mathbf{x}_n)]^\top$, the Gaussian-process posterior for the standardized drag at any test point \mathbf{x}_* has mean and variance

$$\mu(\mathbf{x}_*) = \mathbf{k}_*^\top K^{-1} \mathbf{y}, \quad s^2(\mathbf{x}_*) = \sigma^2 - \mathbf{k}_*^\top K^{-1} \mathbf{k}_*, \quad (15)$$

where $\mathbf{k}_* = [k_\eta(\mathbf{x}_*, \mathbf{x}_1), \dots, k_\eta(\mathbf{x}_*, \mathbf{x}_n)]^\top$ and $K \in \mathbb{R}^{n \times n}$ is the kernel matrix collecting the covariances among the training inputs. To represent small numerical noise and to stabilize the inversion of the covariance matrix, a diagonal term is added and K is defined in practice as $K_{ij} = k_\eta(\mathbf{x}_i, \mathbf{x}_j) + \sigma_n^2 \delta_{ij}$, where δ_{ij} denotes the Kronecker delta and σ_n^2 is an observation noise variance. In the implementation, σ_n^2 is initialized to 10^{-6} with bounds $\sigma_n^2 \in [10^{-12}, 10^{-2}]$, and is learned from the data together with the other kernel hyperparameters.

These kernel and noise parameters are collected in a vector of hyperparameters $\boldsymbol{\eta} = \{\sigma, \{\ell_j\}_{j=1}^8, \sigma_n\}$, which are learned by maximizing the log marginal likelihood [13, 14]:

$$\log p(\mathbf{y} \mid X, \boldsymbol{\eta}) = -\frac{1}{2} \mathbf{y}^\top K^{-1} \mathbf{y} - \frac{1}{2} \log(\det(K)) - \frac{n}{2} \log(2\pi). \quad (16)$$

Once trained, this Gaussian-process surrogate provides a Gaussian predictive distribution for the standardized latent drag $y(\mathbf{x}_*) \mid X, \mathbf{y}, \boldsymbol{\eta} \sim \mathcal{N}(\mu(\mathbf{x}_*), s^2(\mathbf{x}_*))$ for any normalized input \mathbf{x}_* , with mean and variance given by Eq. (15). The corresponding prediction for the drag on the original scale is obtained by the inverse standardization $\tilde{y}(\mathbf{x}_*) = \bar{y} + s_y y(\mathbf{x}_*)$. These predictions serve both as a smooth surrogate of the high-fidelity GSIS evaluations and as the source of the mean and uncertainty information used by the acquisition and engineering refinements in Sections 3.2 and 3.3.

3.2. Acquisition and Scoring: Uncertainty-Guided Selection

To improve surrogate accuracy and guide the search toward low-drag optima, each optimization round proposes four new designs that are predicted by the Gaussian-process model

to be both promising (low predicted drag) and uncertain (high predictive variance). In each round, a finite candidate pool $\mathcal{C} \subset \mathcal{A}$ is generated, and shapes that are not manufacturable or that tend to produce unstable meshes or solver failures are discarded. The remaining feasible candidates are then scored and ranked using the Gaussian-process predictive distribution, and the top four designs are selected.

Let the current training data be $\mathcal{D} = \{(\mathbf{x}_i, y_i)\}_{i=1}^n$ and the best objective value be $y^+ = \min_{1 \leq i \leq n} y_i$. With the Gaussian-process surrogate in Section 3.1, the predictive response at any candidate \mathbf{x} is modeled by a normal random variable $Y(\mathbf{x}) \sim \mathcal{N}(\mu(\mathbf{x}), s^2(\mathbf{x}))$, with μ and s being the predictive mean and standard deviation, respectively. For minimization, the potential gain over the current best is measured by the improvement random variable $I(\mathbf{x}) = \max\{0, y^+ - Y(\mathbf{x})\}$. The corresponding expected improvement (EI) has the closed form [14]:

$$\text{EI}(\mathbf{x}) = (y^+ - \mu(\mathbf{x})) \Phi(z(\mathbf{x})) + s(\mathbf{x}) \phi(z(\mathbf{x})), \quad \text{with } z(\mathbf{x}) = \frac{y^+ - \mu(\mathbf{x})}{s(\mathbf{x})}, \quad (17)$$

where Φ and ϕ denote the standard normal cumulative distribution function and probability density function, respectively.

Since the magnitudes of EI, s , and μ may vary across operating conditions and optimization rounds, these quantities are rescaled within each candidate pool \mathcal{C} to yield comparable, dimensionless scores. Specifically, for $\mathbf{x} \in \mathcal{C}$, the pool-wise min-max normalization is given by

$$\begin{aligned} \widehat{\text{EI}}(\mathbf{x}) &= \frac{\text{EI}(\mathbf{x}) - \min_{\mathbf{u} \in \mathcal{C}} \text{EI}(\mathbf{u})}{\max_{\mathbf{u} \in \mathcal{C}} \text{EI}(\mathbf{u}) - \min_{\mathbf{u} \in \mathcal{C}} \text{EI}(\mathbf{u}) + \varepsilon}, \\ \widehat{s}(\mathbf{x}) &= \frac{s(\mathbf{x}) - \min_{\mathbf{u} \in \mathcal{C}} s(\mathbf{u})}{\max_{\mathbf{u} \in \mathcal{C}} s(\mathbf{u}) - \min_{\mathbf{u} \in \mathcal{C}} s(\mathbf{u}) + \varepsilon}, \\ \widehat{(-\mu)}(\mathbf{x}) &= \frac{-\mu(\mathbf{x}) - \min_{\mathbf{u} \in \mathcal{C}} \{-\mu(\mathbf{u})\}}{\max_{\mathbf{u} \in \mathcal{C}} \{-\mu(\mathbf{u})\} - \min_{\mathbf{u} \in \mathcal{C}} \{-\mu(\mathbf{u})\} + \varepsilon}, \end{aligned} \quad (18)$$

with a small positive ε for numerical stability. The three normalized signals $\widehat{\text{EI}}$, \widehat{s} , and $\widehat{(-\mu)}$ take values in $[0, 1]$ and represent, respectively, improvement potential, uncertainty, and preference for low predicted drag.

For each candidate pool \mathcal{C} , the composite score used in the basic acquisition rule is defined as

$$S_0(\mathbf{x}) = 0.85 \widehat{\text{EI}}(\mathbf{x}) + 0.15 \widehat{s}(\mathbf{x}), \quad (19)$$

where the two weights form a simple convex combination that gives EI primary influence while retaining a modest contribution from posterior uncertainty and their precise values are chosen heuristically.

3.3. Locality Controls for Accelerated Convergence

To improve robustness and accelerate convergence under the limited evaluation budget, several additional controls are imposed on the acquisition scores and candidate generation,

in the spirit of batch designs that promote diversity and trust region strategies for Bayesian optimization [32, 33]. Here the iteration progress $t \in [0, 1]$ is defined as the fraction of completed optimization rounds, and these additional controls are activated only when t exceeds prescribed thresholds.

Firstly, when $t \geq 0.50$, the score in Eq. (19) is modified to introduce a low-mean bias:

$$S(\mathbf{x}) = 0.4S_0(\mathbf{x}) + 0.6[1 - \hat{\mu}(\mathbf{x})]. \quad (20)$$

This promotes candidates with lower predicted drag as the search proceeds, while retaining a nonzero contribution from S_0 so that designs with high EI and uncertainty can still be explored and selected.

Besides, during this selection described in Section 3.2, each new design is further required to keep at least a prescribed distance from all designs that have already entered the batch in the normalized space, so that the limited evaluations are not wasted on nearly duplicate designs. To allow later-stage batches to explore the most promising region more densely and thereby promote convergence, the minimum separation between batch members is gradually reduced as the optimization progresses. Specifically, we prescribe the progress-dependent minimum distance in the normalized design space as

$$\delta(t) = \begin{cases} 0.03, & t < 0.30 \\ 0.02, & 0.30 \leq t < 0.60 \\ 0.01, & t \geq 0.60 \end{cases} \quad (21)$$

A candidate with normalized design vector \mathbf{x} is eligible for inclusion in the batch only if the distance constraint $\|\mathbf{x} - \mathbf{u}_k\|_2 \geq \delta(t)$ is satisfied for all normalized design vectors \mathbf{u}_k of the previously selected batch members.

Finally, when evidence for a promising region becomes strong, sampling from the global box is further restricted to an axis-aligned box around the current best designs. Specifically, when $t \geq 0.50$ and at least ten ground-truth evaluations are available, let \mathcal{S} denote the set of the ten designs with the smallest objective values. For each design coordinate j , we define

$$[\text{lo}_{\text{eff},j}, \text{hi}_{\text{eff},j}] = \left[\min_{\mathbf{x} \in \mathcal{S}} x_j, \max_{\mathbf{x} \in \mathcal{S}} x_j \right], \quad (22)$$

where x_j denotes the j th component of a design vector \mathbf{x} . Thus $\text{lo}_{\text{eff},j}$ and $\text{hi}_{\text{eff},j}$ are the coordinate-wise minima and maxima over the ten best designs and act as effective lower and upper bounds along coordinate j for candidate generation in the current round. The resulting local box is used only for candidate generation, while the Gaussian-process coordinates and normalization remain unchanged so that the surrogate model is trained and queried on a consistent global input space. As the optimization progresses and the membership of \mathcal{S} evolves, these bounds are recomputed, so that the sampling region is dynamically adapted and gradually contracted around the region containing the currently best designs, which promotes faster convergence of the overall optimization.

Table 1: Objective D for NACA 0012 at $\text{Ma} = 2$ under four representative Knudsen numbers. Grids G1/G2/G3 use 201/301/401 chord-wise nodes on the upper and lower surfaces, 25/35/50 near-wall layers with first-layer thicknesses $5 \times 10^{-4}c/3.5 \times 10^{-4}c/2.5 \times 10^{-4}c$ and growth factors 1.04/1.035/1.03; the far-field radius and sparsity are fixed at $10c$ and 40 nodes.

Kn	G1 (coarse)	G2 (medium)	G3 (fine)
0.001	0.4466	0.4427	0.4380
0.01	0.8002	0.7936	0.7889
0.1	1.5559	1.5509	1.5495
1.0	2.1730	2.1720	2.1713

4. Numerical results

In this section, a mesh-independence study is first conducted to verify the numerical setup, followed by validation of the surrogate-assisted optimization framework against reference solutions. Then, the framework is applied to identify, at $M_\infty = 2$ and $M_\infty = 4$, drag-minimizing airfoils over a wide range of Knudsen numbers. Finally, the resulting optimal designs are used to characterize their Knudsen- and Mach-number dependence through the behavior of drag and key geometric features. In all test cases, the GSIS solver is run with identical numerical settings, except that the velocity-space domain and discretization are adjusted with the freestream Mach number, as detailed in Section 2.4.

4.1. Mesh-independence verification

We first verify mesh independence of the objective D using NACA 0012 at $\text{Ma} = 2$ under the four representative Knudsen numbers listed in Table 1. Numerically, D decreases monotonically from G1 (coarse) to G3 (fine) for all four Knudsen numbers, with the coarse-to-fine change remaining below about 2% and the medium-to-fine change decreasing from approximately 1.1% at $\text{Kn} = 10^{-3}$ to 0.03% at $\text{Kn} = 1$. In view of the small coarse-to-fine differences (at most about 2%) and the large number of samples required in the optimization studies, the coarse grid G1 is adopted in the remainder of this work.

4.2. Validation of the optimization framework

To validate the surrogate-assisted optimization framework, shape optimizations are performed at $\text{Kn} = 0.01$ and $\text{Kn} = 0.50$ with a freestream Mach number of $M_\infty = 2$, and the resulting optimal airfoils are compared with the adjoint-based designs [34]. To avoid inconsistencies in objective definition, nondimensionalization, and boundary modeling, we do not compare absolute drag values here, but focus on the changes in geometry and flow field from the initial to the optimized airfoils.

As summarized in Table 2, the optimized airfoils reduce the drag by about 11% at $\text{Kn} = 0.01$ and 5% at $\text{Kn} = 0.50$. In both cases, candidates very close to the final optimum already appear after about 150 samples. The eventual choice of 240 samples (see Section 3) is intended to improve statistical robustness, so that the ten lowest-drag airfoils in the computed set are nearly indistinguishable in shape.

Table 2: Summary of surrogate-assisted airfoil optimizations at $Ma = 2$. Each airfoil mesh contains some 2×10^4 cells. The “Time” column reports the total wall-clock time for all 240 samples per case on 60 cores, corresponding to roughly 2 min per steady GSIS solve [27] at $Kn = 0.01$ and 3 min at $Kn = 0.50$.

Kn	D (initial)	D (optimized)	Reduction	Time
0.01	0.8054	0.7151	11.2%	8 hours
0.50	2.0670	1.9706	4.7%	12 hours

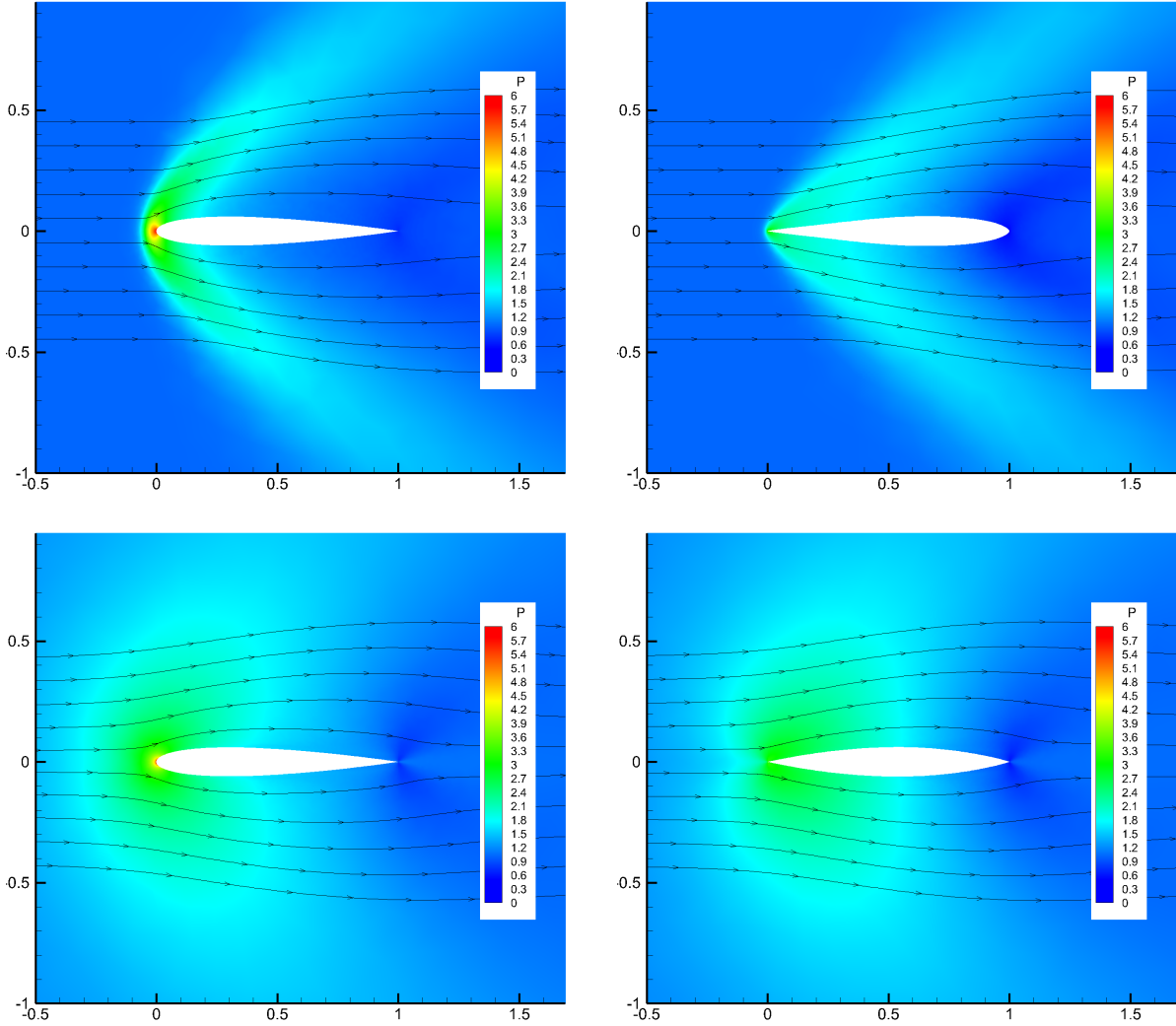


Figure 3: Flowfield comparison at $Ma = 2$ between the initial (left column) and optimized (right column) airfoils. The Knudsen numbers are 0.01 and 0.50 in the top and bottom rows, respectively.

Figure 3 compares the pressure fields and streamlines around the initial and optimized airfoils. For $Kn = 0.01$, the initial airfoil exhibits a large high-pressure stagnation region near the leading edge and a narrow, steep pressure gradient along the upper surface. After

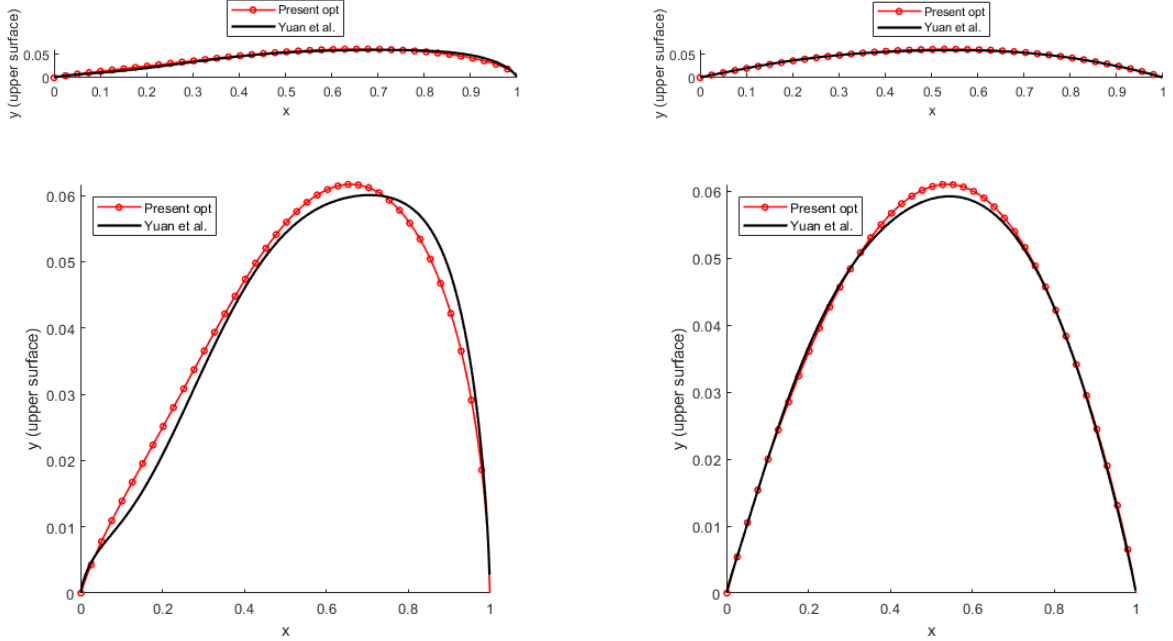


Figure 4: Geometry-only comparison between our optimized thickness distributions and the shape optimization method [34] at $Ma = 2$. First row: physical-scale view at $Kn = 0.01$ (left) and $Kn = 0.50$ (right). Second row: vertically magnified view.

optimization, the leading-edge high-pressure region shrinks, isobars in the upper-surface neighborhood become more widely spaced, and streamlines turn less sharply around the nose and trailing edge, aligning more closely with the freestream. For $Kn = 0.50$, the initial airfoil still produces a relatively broad medium-to-high-pressure region ahead of the leading edge and noticeable streamline turning around the nose and trailing edge. After optimization, this elevated-pressure patch contracts, the isobars around the upper surface become smoother and more evenly spaced, and the low-pressure pocket near the trailing edge is regularized. In both cases, the optimized shapes weaken excessive compression and flow turning near the nose, effectively straightening the main flow passage and reducing drag.

Figure 4 compares our optimal airfoils against those of the adjoint shape optimization method [34]. For $Kn = 0.01$, the two $y_u(x)$ curves almost coincide at the leading and trailing edges; in the main thickness region $x \approx 0.2$ – 0.7 , the present optimum lies slightly above that of the adjoint optimization with nearly identical peak location. The difference arises from the different kinetic models used: our method employs the modified Rykov kinetic model for polyatomic gases, whereas Ref. [34] uses the BGK model for monoatomic gases. Consequently, the Prandtl numbers differ, leading to differences in the predicted temperature field, which in turn slightly affect the drag calculation. For $Kn = 0.50$, the discrepancy is further reduced: the leading edge, peak, and trailing edge nearly coincide.

Taken together, the above comparisons show that the present optimization framework

can automatically yield drag-reducing, geometrically smooth optimal airfoils for $\text{Ma} = 2$ at $\text{Kn} = 0.01$ and $\text{Kn} = 0.50$, while remaining consistent with existing reference results. These findings provide a starting point for extending the optimization framework to broader sets of operating conditions.

4.3. Knudsen-number dependence of optimal airfoils at $M_\infty = 2$

Figure 5 shows the optimal airfoils obtained with our optimization framework at $M_\infty = 2$ over 11 different Knudsen numbers, together with the initial NACA0012 airfoil. It can be seen that, as Kn varies, the optimal shapes exhibit systematic shifts in peak thickness, peak-thickness location, and aft loading relative to the baseline section. To quantify these trends, we examine, as functions of Kn , the total nondimensional streamwise force and the corresponding relative drag reduction, the pressure and viscous contributions to the drag and their respective fractions, as well as several geometric indicators such as the maximum thickness and its chordwise position.

Figure 6 shows that, as Kn increases, the drag force F_d for both the baseline and optimized airfoils increases monotonically. Although the optimized airfoils consistently exhibit lower drag than the baseline configuration, they follow the same overall trend. Using “ini” and “opt” to indicate the baseline and optimized airfoils, respectively, the relative drag reduction

$$\eta_{\text{red}} = \frac{F_d^{\text{ini}} - F_d^{\text{opt}}}{F_d^{\text{ini}}} \quad (23)$$

is largest in the weakly rarefied regime, reaching about 30% at the smallest Kn , then decays rapidly with Kn and levels off near 5% at medium to high Kn . Thus shape optimization yields substantial drag reductions in near-continuum flows but only modest incremental benefits once the flow enters the slip–transition or strongly rarefied regime.

To clarify the origin of this behavior, Fig. 7 decomposes the total force into pressure drag p_x and viscous drag $F_{d,\tau}$. For the baseline, p_x^{ini} varies only mildly with Kn and stays at a roughly constant level, while $F_{d,\tau}^{\text{ini}}$ increases significantly and is mainly responsible for the growth of F_d . This is reflected in the pressure fraction ϕ_p and viscous fraction ϕ_τ :

$$\phi_p = \frac{p_x}{F_d}, \quad \phi_\tau = \frac{F_{d,\tau}}{F_d}, \quad (24)$$

for which $\phi_p^{\text{ini}} \approx 0.6$ at small Kn and decreases to about 0.1–0.2 at large Kn , whereas ϕ_τ^{ini} increases from about 0.4 to nearly 0.9, indicating that the dominant contribution to the drag shifts from pressure to viscous effects. The optimized airfoils reduce p_x^{opt} by roughly 30–50% across the entire Kn range, while the changes in $F_{d,\tau}^{\text{opt}}$ remain moderate: it is slightly larger than $F_{d,\tau}^{\text{ini}}$ at small Kn , and comparable to or slightly smaller than the baseline at medium and high Kn . Net drag reduction is therefore achieved mainly by weakening the pressure contribution while keeping viscous drag broadly similar.

Figure 8 summarizes the geometric response of the optimal airfoils as Kn varies. As Kn increases, the chordwise location of maximum thickness $x_{t,\text{max}}/c$ moves forward from about

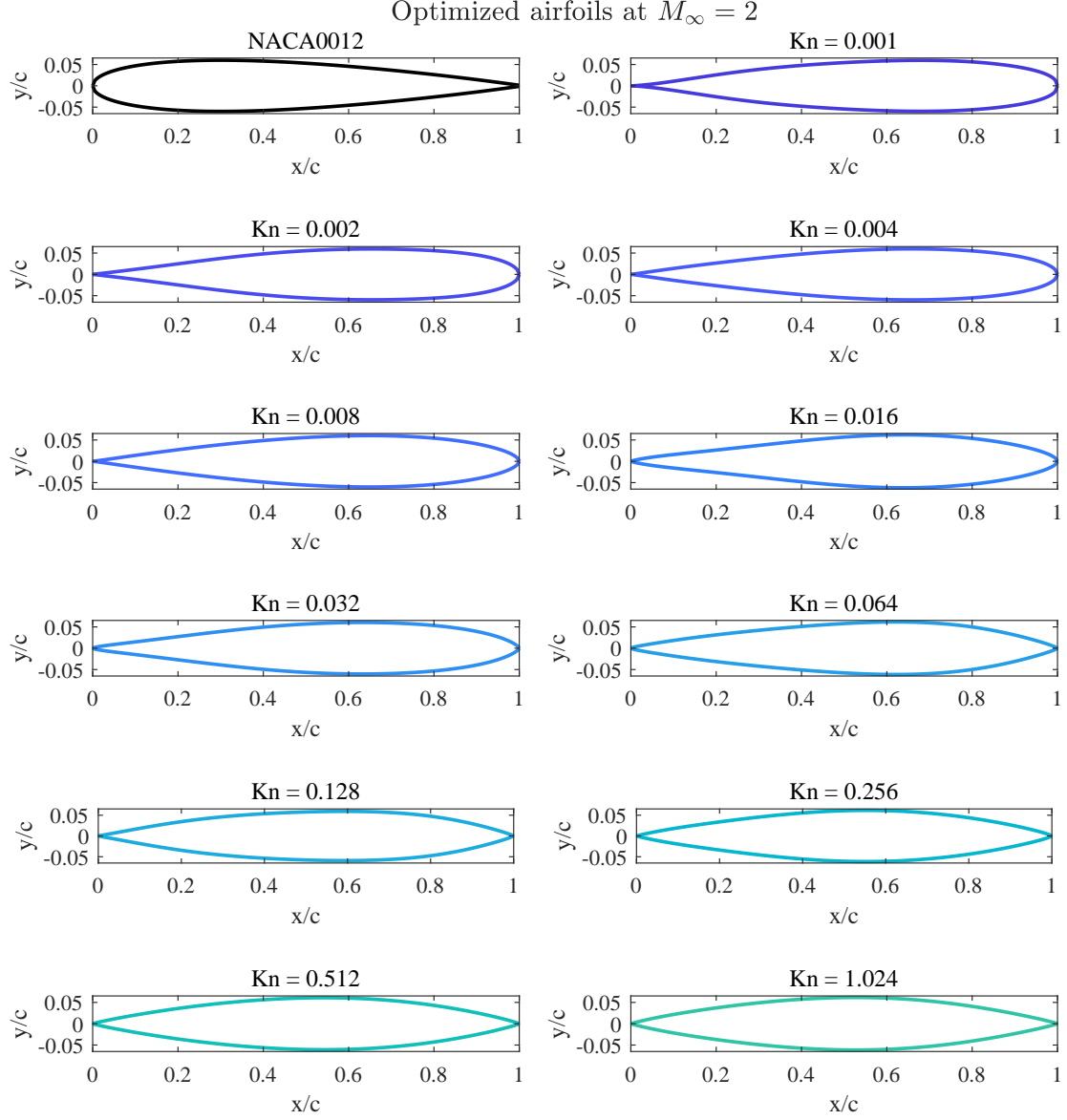


Figure 5: Optimized airfoil shapes at $M_\infty = 2$ at 11 different Knudsen numbers. The flow is from left to right.

0.68 to about 0.53, which helps alleviate pressure recovery and viscous loading in the rear part. Let A_{tot} denote the total sectional thickness area and A_{aft} the portion of this area downstream of mid-chord ($x/c > 0.5$), it can be seen that the aft half-chord thickness-area fraction $A_{\text{aft}}/A_{\text{tot}}$ decreases monotonically with Kn, from above 60% at small Kn to about 50% at large Kn. Combined with the forward shift of $x_{t,\text{max}}/c$, this indicates that the optimal thickness distribution contracts toward the front as Kn increases, and the aft body becomes relatively thinner.

To track how the nose and tail geometries evolve with Kn without entangling this measure

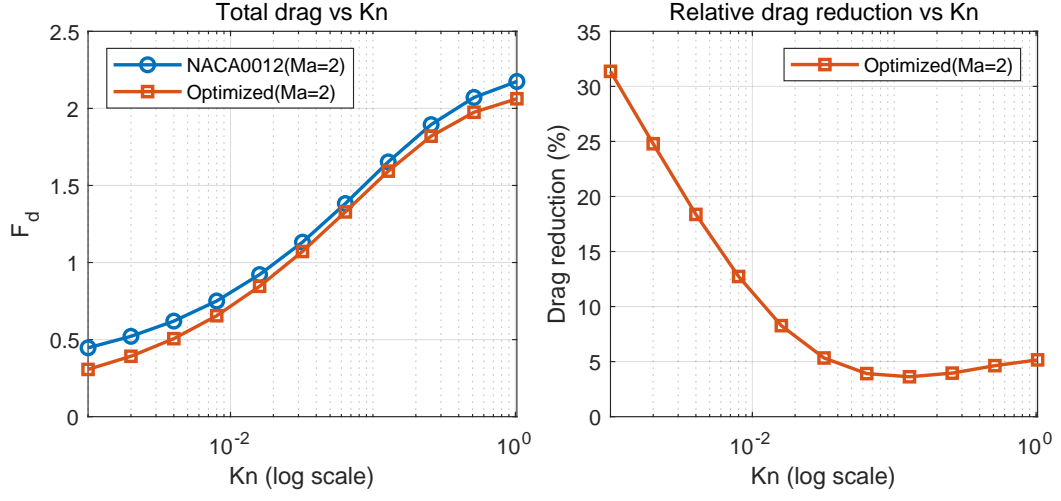


Figure 6: Variation of the total nondimensional streamwise force F_d and the relative drag reduction with Knudsen number for the baseline NACA0012 and the optimized airfoil at $M_\infty = 2$.

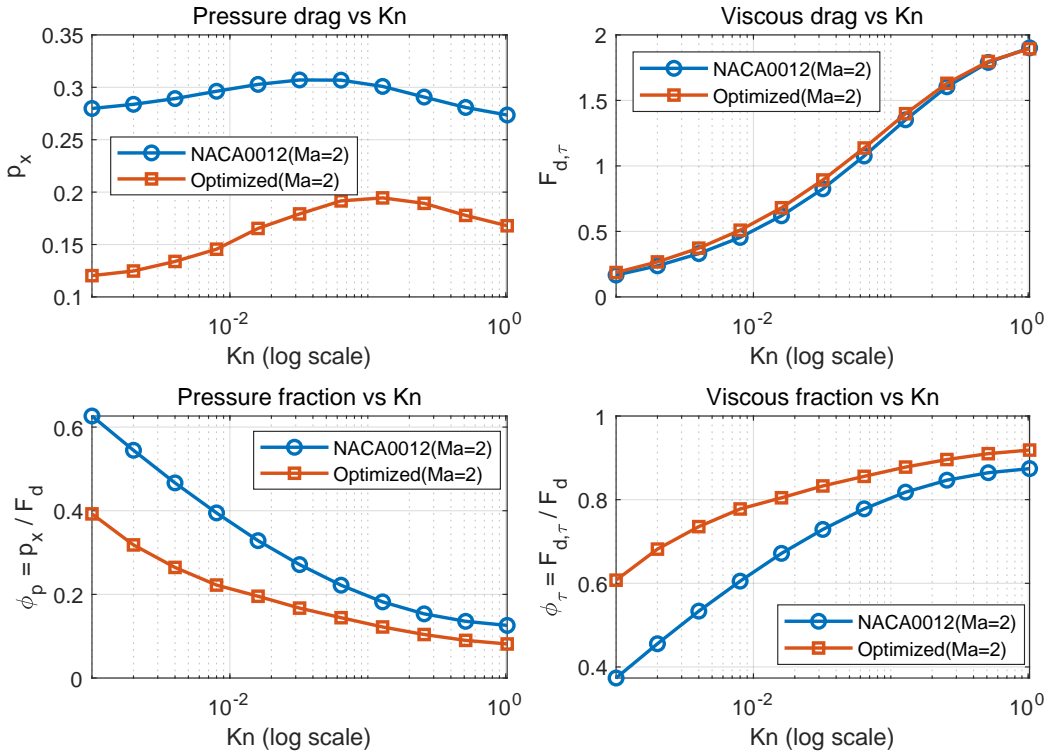


Figure 7: Decomposition of the total streamwise force into pressure drag p_x and viscous drag $F_{d,\tau}$, and the corresponding fractions, as functions of Knudsen number at $M_\infty = 2$.

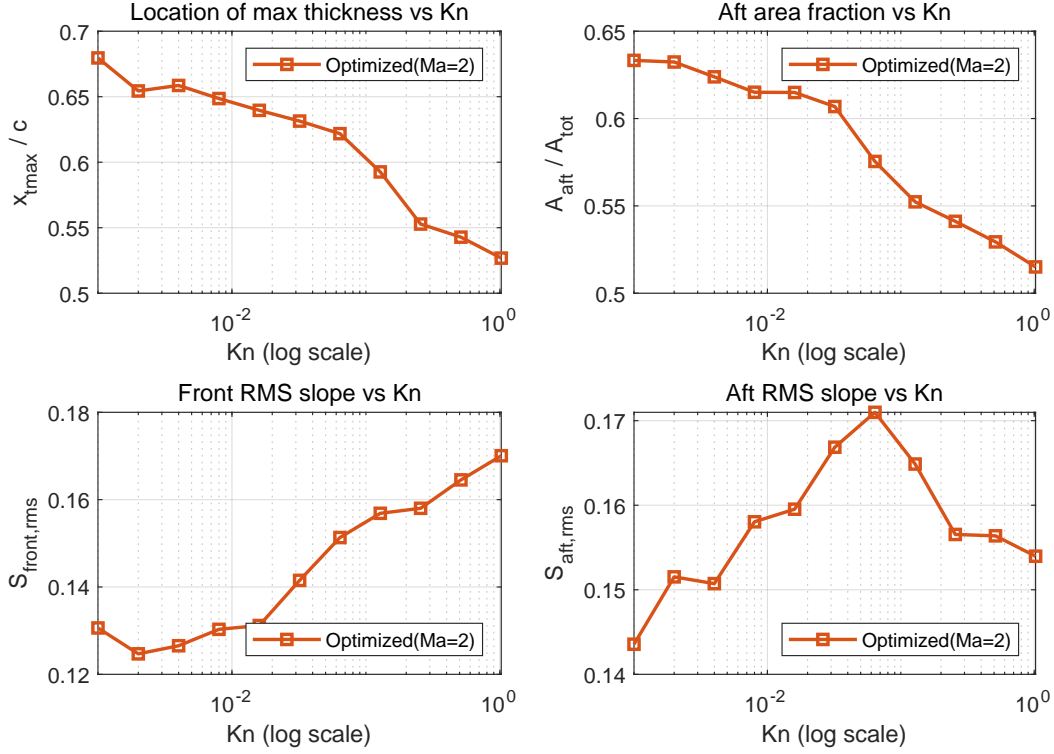


Figure 8: Geometric response of the optimized airfoil at $M_\infty = 2$, including the chord-wise location of maximum thickness $x_{t\max}/c$, the after half-chord thickness-area fraction $A_{\text{aft}}/A_{\text{tot}}$, and the RMS slopes in the leading-edge and after-body regions, as functions of Knudsen number.

with the shifting location of maximum thickness, we introduce two simple root-mean-square (RMS) slope indicators on fixed chordwise windows. These windows are chosen empirically to sample the leading-edge and aft-body neighborhoods (rather than the mid-chord region where the surface is nearly flat) and to exclude the very last grid points near the trailing edge where numerical noise can be more pronounced. For a set of chordwise grid points $\{x_i\}_{i=1}^N$, the front-region RMS slope $S_{\text{front,rms}}$ and aft-region RMS slope $S_{\text{aft,rms}}$ are then defined as

$$S_{\text{front,rms}} = \sqrt{\frac{1}{N_{\text{front}}} \sum_{i: 0 \leq x_i/c \leq 0.3} \left(\frac{dy_u}{dx} \right)^2 \bigg|_{x_i}}, \quad S_{\text{aft,rms}} = \sqrt{\frac{1}{N_{\text{aft}}} \sum_{i: 0.6 \leq x_i/c \leq 0.98} \left(\frac{dy_u}{dx} \right)^2 \bigg|_{x_i}}, \quad (25)$$

where $y_u(x)$ is the upper-surface ordinate and N_{front} and N_{aft} are the numbers of grid points in these two windows. These RMS slopes serve as simple indicators of local surface steepness and small-scale waviness in the leading-edge and aft-body regions. It can be seen from Fig 8 that $S_{\text{front,rms}}$ increases mildly with Kn (from about 0.13 to 0.17), indicating a progressively steeper leading-edge region. In contrast, $S_{\text{aft,rms}}$ first rises from about 0.145 to a peak of roughly 0.18 at intermediate Kn and then decreases slightly to around 0.16 at $\text{Kn} = 1$, meaning that the aft section exhibits the steepest thickness decay at intermediate Kn.

Overall, Figs. 6–8 show that, at $M_\infty = 2$, the optimal airfoils across the considered Kn range form a smooth, single-peaked thickness family and adapt through three coupled trends. First, the total drag increases and becomes increasingly viscous-dominated as Kn grows. Second, optimization at each operating point primarily reduces pressure drag while only moderately adjusting viscous drag, with the relative benefit largest at small Kn. Third, the optimal airfoils show a gradual evolution from a clearly aft-loaded shape with a more bulged tail at small Kn toward a family where the thickness peak moves forward and the aft section is thinner and more front-loaded.

4.4. Mach-number dependence: optimal airfoils at $M_\infty = 4$

Figure 9 shows the optimal airfoils obtained with our optimization framework at $M_\infty = 4$ over 11 different Knudsen numbers, whose geometric evolution with Kn broadly mirrors the $M_\infty = 2$ case but also exhibits some differences.

Figure 10 shows that, at $M_\infty = 4$, the total drag F_d of both the baseline and optimized airfoils still increases monotonically with Kn, but with substantially larger magnitude than those of $M_\infty = 2$ due to stronger shocks and compression. For the optimal airfoils, the relative drag reduction reaches about 40–50% at low Kn, noticeably exceeding $\approx 30\%$ at $M_\infty = 2$, then drops rapidly and approaches a common level of roughly 5% at medium to high Kn for both Mach numbers. Thus, in strongly rarefied or slip-transition regimes, the additional room for drag reduction via shape optimization is similarly limited at $M_\infty = 2$ and 4.

Figure 11 shows that, for the baseline NACA0012 airfoil at $M_\infty = 4$, the pressure contribution p_x^{ini} stays close to 1.0 over the considered Knudsen numbers, varying only within roughly $\pm 10\%$ as Kn increases. In contrast, the viscous contribution $F_{d,\tau}^{\text{ini}}$ grows rapidly from about 0.3 at $\text{Kn} = 10^{-2}$ to nearly 5 at $\text{Kn} = 1$, and is therefore the main driver of the increase in the total drag F_d , consistent with the $M_\infty = 2$ case. After optimization, p_x^{opt} is clearly reduced at all Kn, taking values of about 0.3–0.5, with the largest relative reduction at low Kn. The viscous contribution $F_{d,\tau}^{\text{opt}}$ is slightly larger than $F_{d,\tau}^{\text{ini}}$ at small Kn, but becomes comparable to or marginally smaller than the baseline at intermediate and high Kn. This behaviour again indicates that the optimization is achieved primarily by weakening the pressure component of the drag.

The lower panels of Fig. 11 compare the pressure fraction $\phi_p = p_x/F_d$ and viscous fraction $\phi_\tau = F_{d,\tau}/F_d$ across Mach numbers. For the baseline at $M_\infty = 4$, $\phi_p^{\text{ini}} \approx 0.6$ –0.7 at small Kn and decreases to about 0.1–0.2 at large Kn, indicating that, as rarefaction strengthens, the drag again shifts from being predominantly pressure-driven to predominantly viscous-driven, consistent with the $M_\infty = 2$ case. Compared with the baseline, the optimized airfoils at both Mach numbers exhibit reduced ϕ_p^{opt} and increased ϕ_τ^{opt} . In most of the Kn range, the optimized design at $M_\infty = 2$ attains a lower ϕ_p and higher ϕ_τ than the optimized design at $M_\infty = 4$, while the latter lies between the $M_\infty = 2$ optimum and the $M_\infty = 4$ baseline. Because the baseline pressure contribution is larger at $M_\infty = 4$, there is more room to redistribute drag away from the pressure component, which helps explain the stronger relative drag reduction achieved at low Kn.

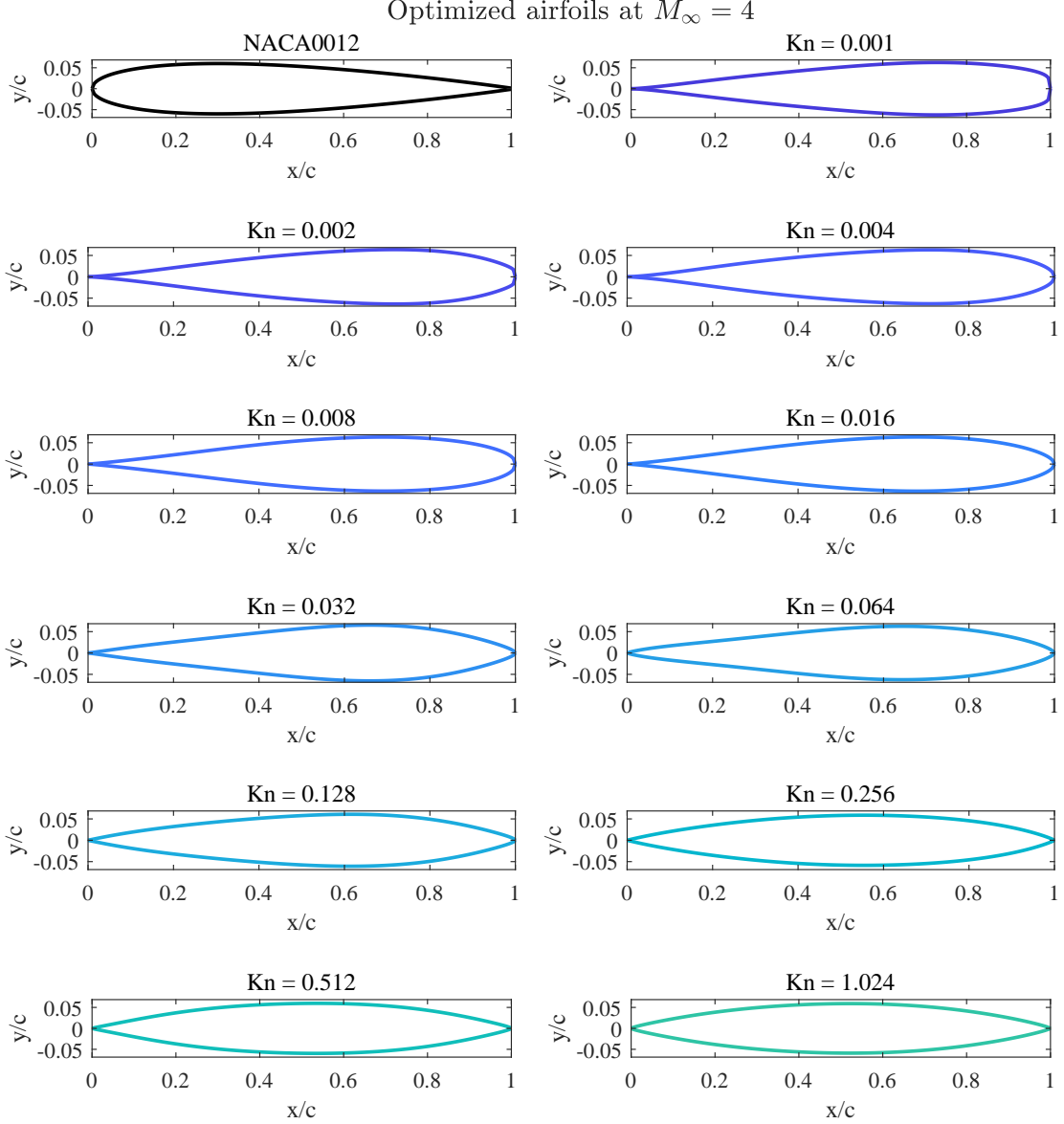


Figure 9: Optimized airfoil shapes at $M_\infty = 4$ at 11 different Knudsen numbers, plotted with the same scaling as Figure 5.

Figure 12 summarizes the geometric response of the optimal airfoils at $M_\infty = 2$ and $M_\infty = 4$ as Kn varies. At both Mach numbers, the maximum-thickness location $x_{t\max}/c$ shifts smoothly from a clearly after-biased position toward mid-chord with increasing Kn . At small Kn the peak at $M_\infty = 4$ lies further aft than at $M_\infty = 2$, and its forward migration is more pronounced; in the high- Kn regime the two peak locations become close, with $M_\infty = 4$ still slightly trailing. Consistently, the after half-chord thickness-area fraction $A_{\text{aft}}/A_{\text{tot}}$ is higher at $M_\infty = 4$ than at $M_\infty = 2$ at low Kn , reflecting a more strongly after-loaded distribution that helps alleviate leading-edge shocks, and decreases toward similar levels as

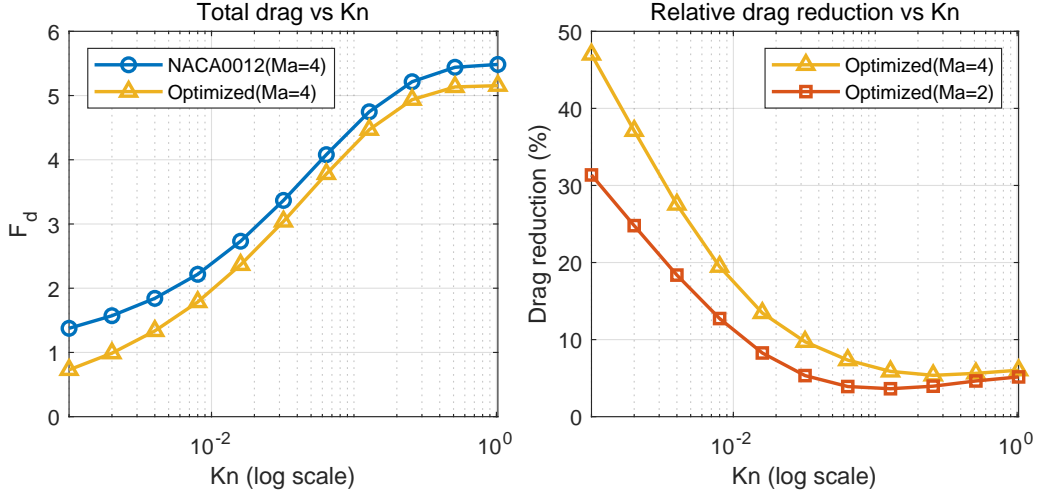


Figure 10: Variation of the total nondimensional streamwise force F_d and the relative drag reduction with Knudsen number for the baseline NACA0012 and the optimized airfoil at $M_\infty = 4$. The right panel also shows the drag-reduction curve of the optimized airfoil at $M_\infty = 2$ for comparison.

Kn increases.

The front- and aft-region RMS slopes further clarify the local geometric trends. As Kn increases, the front-region RMS slope $S_{\text{front,rms}}$ grows steadily at both Mach numbers, indicating a progressively steeper increase in thickness from the leading edge toward mid-chord, with slightly larger values reached at $M_\infty = 4$. The aft-region RMS slope $S_{\text{aft,rms}}$ rises with Kn and then decreases mildly at the largest Kn for both cases, but its variation is more pronounced at $M_\infty = 4$, indicating a stronger thickness decay and more intensive aft-body shaping to accommodate the stronger shocks and rarefaction effects at higher Mach number.

Taken together with the forward shift of $x_{t,\text{max}}/c$ and the reduction in $A_{\text{aft}}/A_{\text{tot}}$, these trends suggest that, while both Mach numbers share a smooth, single-peaked thickness family, the optimal designs at $M_\infty = 4$ rely more heavily on aft-loaded thickness at low Kn and on a stronger forward redistribution of thickness and aft-body steepness as Kn increases, consistent with the pressure-to-viscous rebalancing seen in the drag decomposition.

5. Conclusions

In summary, we have developed a solver-in-the-loop shape-optimization framework for symmetric, thickness-only airfoils operating in rarefied flows. The framework combines a regularized CST parameterization with a surrogate-assisted Bayesian optimizer and the efficient kinetic solver GSIS. This combination enables the systematic identification of drag-minimizing airfoil designs over a range of rarefied-flow conditions under a limited evaluation budget, while simple geometric filters and admissibility constraints help exclude nonphysical shapes and maintain numerical robustness.

The results at $M_\infty = 2$ and $M_\infty = 4$ show that, as the flow transitions from the near-continuum to the strongly rarefied regime, the total nondimensional streamwise force grows

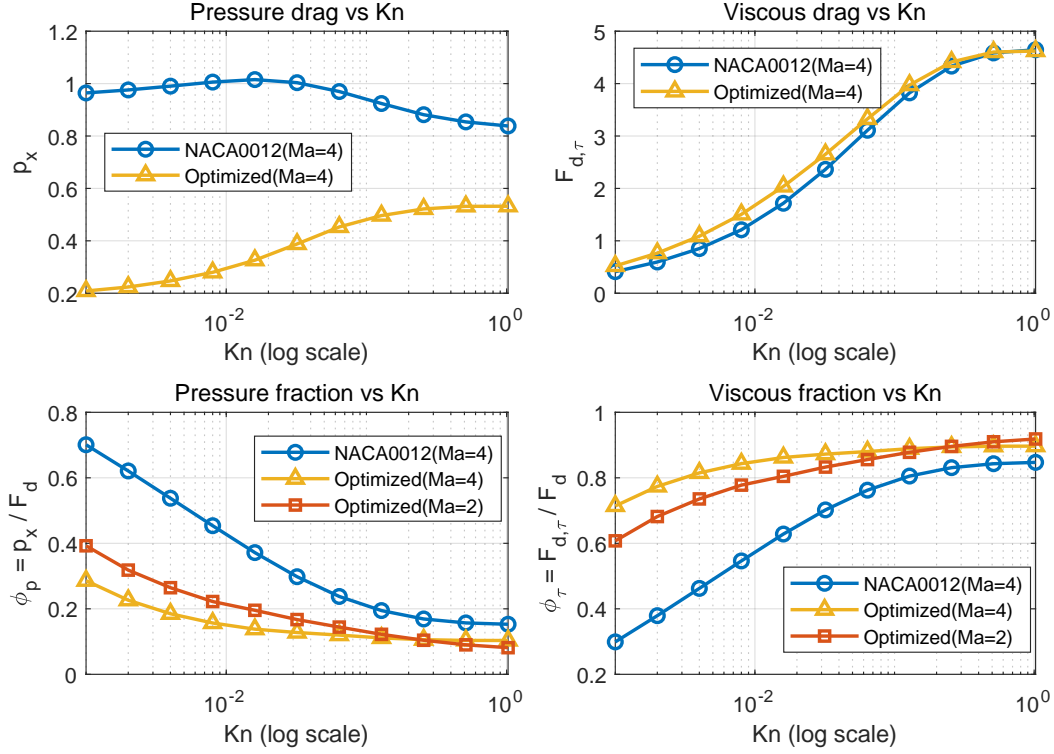


Figure 11: Decomposition of the total streamwise force into pressure drag p_x and viscous drag $F_{d,\tau}$ at $M_\infty = 4$, together with the corresponding fractions. The lower panels also include the fractions of the optimized airfoil at $M_\infty = 2$ for comparison.

markedly and the drag changes from being pressure-dominated to viscous-dominated. Shape optimization consistently yields a net drag reduction across all Kn and both Mach numbers. In the weakly rarefied regime, the relative reduction reaches about 30% at $M_\infty = 2$ and up to roughly 40–50% at $M_\infty = 4$, reflecting the larger penalty of shock-related pressure drag at higher Mach number. As the flow enters the slip–transition and strongly rarefied regimes, the achievable reduction decreases to a few percent and becomes comparable at the two Mach numbers. A decomposition of the optimized designs shows that, in all cases, the drag reduction is achieved primarily by substantially reducing the pressure contribution, while keeping the viscous drag nearly unchanged or only modestly altered. Consequently, at fixed M_∞ the optimal airfoils systematically shift the aerodynamic load from the pressure component toward the viscous component while still lowering the total drag, and the stronger shock system at $M_\infty = 4$ enlarges the initial pressure contribution and thus the scope for such pressure-to-viscous rebalancing, explaining the larger relative gains observed in the weakly rarefied regime.

The geometric response of the optimal airfoil family provides a consistent picture across both Mach numbers. Over the considered Knudsen numbers, the optimal airfoils retain a smooth, single-peaked thickness profile, but show a systematic forward shift of the maximum-

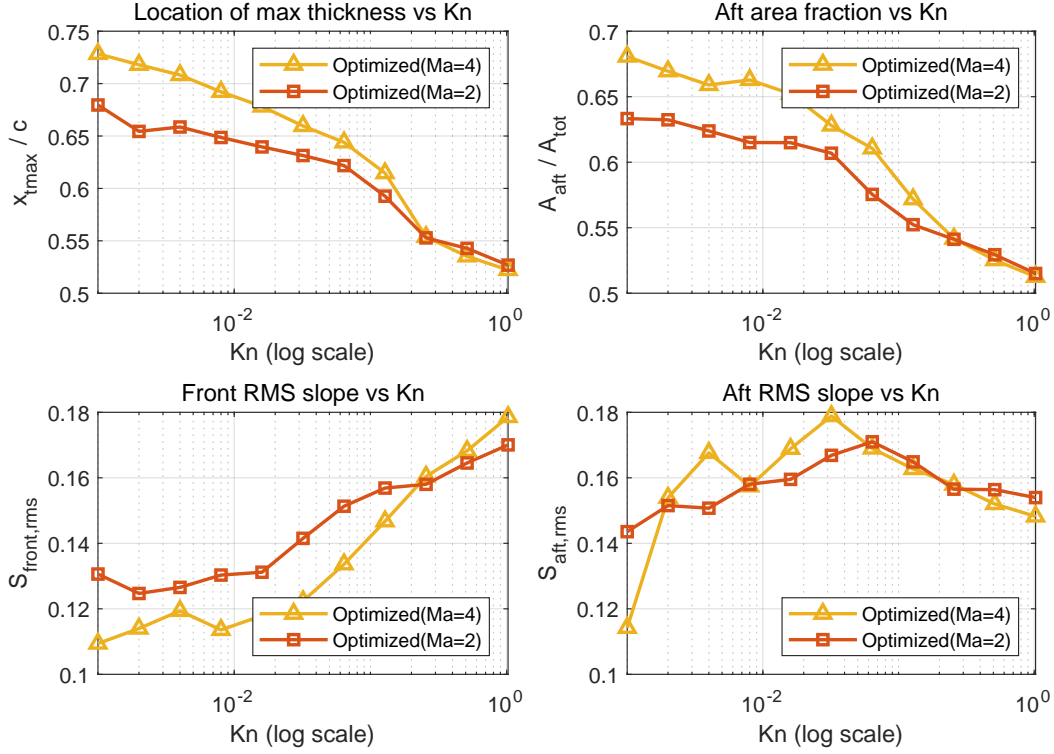


Figure 12: Geometric response of the optimized airfoils at $M_\infty = 2$ and $M_\infty = 4$ as functions of Knudsen number, including the chord-wise location of maximum thickness x_{tmax}/c , the after half-chord thickness-area fraction A_{aft}/A_{tot} , and the RMS slopes in the leading-edge and after-body regions.

thickness location and a gradual transfer of thickness area from the aft half-chord toward the mid-chord region. At low Kn , the optimal airfoils are clearly aft-loaded: the thickness peak lies downstream of mid-chord and more than half of the thickness area is located in the aft half-chord, especially at $M_\infty = 4$, where a more aft-loaded distribution helps to accommodate the stronger shock system. As Kn increases, the thickness peak moves smoothly toward mid-chord and the aft half-chord carries a smaller fraction of the total thickness area, so that the chordwise load distribution becomes more front-loaded. At the same time, the thickness variation in the leading-edge region becomes progressively steeper, whereas in the aft section it is most pronounced at intermediate Kn .

Taken together, these findings indicate that, over the explored (M_∞, Kn) range, the optimal airfoils form a coherent, rarefaction-aware shape family. They maintain a regularized, single-peaked thickness profile, reduce the total drag mainly by weakening the pressure contribution while only modestly changing the viscous contribution, and respond to changes in both Mach and Knudsen numbers through smooth and interpretable geometric shifts in peak location, thickness distribution, and local surface steepness.

Beyond the specific numerical values, the study demonstrates that a tightly integrated workflow—combining CST-based regularization, a carefully constrained admissible set, a

Gaussian-process surrogate with expected-improvement acquisition, and a GSIS kinetic solver—can robustly handle regimes in which neither classical Navier–Stokes models nor purely stochastic particle methods are individually efficient, and offers a practical basis for extending the present approach to cambered sections, three-dimensional wings, and multi-objective formulations in rarefied aerodynamic design.

Declaration of competing interest

The authors declare that they have no known competing financial interests or personal relationships that could have appeared to influence the work reported in this paper.

Acknowledgments

This work is supported by the National Natural Science Foundation of China (12402388). The authors acknowledge the computing resources from the Center for Computational Science and Engineering at the Southern University of Science and Technology.

References

- [1] Henning Struchtrup. *Macroscopic Transport Equations for Rarefied Gas Flows: Approximation Methods in Kinetic Theory*. Springer, Berlin, Heidelberg, 2005.
- [2] Cem Pekardan and Alina Alexeenko. Rarefaction effects for transonic airfoil flows at low Reynolds numbers. *AIAA Journal*, 56(2):765–779, 2018. doi: 10.2514/1.J056051.
- [3] Andrew J Lofthouse, Iain D Boyd, and Michael J Wright. Effects of continuum breakdown on hypersonic aerothermodynamics. *Physics of Fluids*, 19(2), 2007.
- [4] John D. Anderson. *Hypersonic and High-Temperature Gas Dynamics*. AIAA, Reston, VA, 2 edition, 2006.
- [5] Sinan Eyi, Kyle M. Hanquist, and Iain D. Boyd. Shape optimization of reentry vehicles to minimize heat loading. *Journal of Thermophysics and Heat Transfer*, 33(3):785–796, 2019.
- [6] Antony Jameson. Aerodynamic shape optimization techniques based on control theory. In *36th AIAA Aerospace Sciences Meeting and Exhibit*, 1998. AIAA Paper 98-2538.
- [7] Michael B. Giles and N. A. Pierce. An introduction to the adjoint approach to design. *Flow, Turbulence and Combustion*, 65(3):393–415, 2000.
- [8] Bijan Mohammadi and Olivier Pironneau. *Applied Shape Optimization for Fluids*. Numerical Mathematics and Scientific Computation. Oxford University Press, 2009.
- [9] Akihito Sato, Takayuki Yamada, Kazuhiro Izui, and Shinji Nishiwaki. A topology optimization method in rarefied gas flow problems using the Boltzmann equation. *Journal of Computational Physics*, 395:135–164, 2019.

- [10] Kaiwen Guan, Kei Matsushima, Yuki Noguchi, and Takayuki Yamada. Topology optimization for rarefied gas flow problems using density method and adjoint ip-DSMC. *Journal of Computational Physics*, 474:111788, 2023. doi: 10.1016/j.jcp.2022.111788.
- [11] Russell Caflisch, Dmitry Silantyev, and Yunan Yang. Adjoint DSMC for nonlinear Boltzmann equation constrained optimization. *Journal of Computational Physics*, 439:110404, 2021.
- [12] Ruifeng Yuan and Lei Wu. A design optimization method for rarefied and continuum gas flows. *Journal of Computational Physics*, 517:113366, 2024.
- [13] Carl Edward Rasmussen and Christopher K. I. Williams. *Gaussian Processes for Machine Learning*. MIT Press, Cambridge, MA, 2006.
- [14] Donald R. Jones, Matthias Schonlau, and William J. Welch. Efficient global optimization of expensive black-box functions. *Journal of Global Optimization*, 13(4):455–492, 1998.
- [15] Luis Miguel Rios and Nikolaos V. Sahinidis. Derivative-free optimization: a review of algorithms and comparison of software implementations. *Journal of Global Optimization*, 56(3):1247–1293, 2013.
- [16] Jacob Gardner, Matt Kusner, Zhixiang Xu, Kilian Q. Weinberger, and John P. Cunningham. Bayesian optimization with inequality constraints. In *Proceedings of the 31st International Conference on Machine Learning (ICML)*, volume 32 of *Proceedings of Machine Learning Research*, pages 937–945. PMLR, 2014.
- [17] Javier González, Zhenwen Dai, Philipp Hennig, and Neil D. Lawrence. Batch bayesian optimization via local penalization. In *Proceedings of the 19th International Conference on Artificial Intelligence and Statistics (AISTATS)*, volume 51 of *Proceedings of Machine Learning Research*, pages 648–657. PMLR, 2016.
- [18] Graeme A. Bird. *Molecular Gas Dynamics and the Direct Simulation of Gas Flows*. Clarendon Press, Oxford, 1994. ISBN 9780198561958.
- [19] Mikhail S. Ivanov and Sergey F. Gimelshein. Computational hypersonic rarefied flows: Particle methods and DSMC. *Annual Review of Fluid Mechanics*, 30:469–505, 1998.
- [20] Kun Xu. *Direct Modeling for Computational Fluid Dynamics: Construction and Application of Unified Gas-Kinetic Schemes*. World Scientific, Singapore, 2015.
- [21] Brenda M. Kulfan. Universal parametric geometry representation method. *Journal of Aircraft*, 45(1):142–158, 2008.
- [22] Raymond M. Hicks and P. A. Henne. Wing design by numerical optimization. *Journal of Aircraft*, 15(7):407–412, 1978.

- [23] Jamshid A. Samareh. Survey of shape parameterization techniques for high-fidelity multidisciplinary shape optimization. *AIAA Journal*, 39(5):877–884, 2001.
- [24] Ziming Lyu, Gaetan J. Kenway, and Joaquim R. R. A. Martins. Aerodynamic shape optimization investigations of the common research model wing. *AIAA Journal*, 52(10):2297–2310, 2014.
- [25] Wei Su, Lianhua Zhu, and Lei Wu. Fast convergence and asymptotic preserving of the general synthetic iterative scheme. *SIAM Journal on Scientific Computing*, 42(6):B1517–B1540, 2020.
- [26] Lianhua Zhu, Xingcai Pi, Wei Su, Zhi-Hui Li, Yonghao Zhang, and Lei Wu. General synthetic iterative scheme for nonlinear gas kinetic simulation of multi-scale rarefied gas flows. *Journal of Computational Physics*, 430:110091, 2021. doi: 10.1016/j.jcp.2020.110091.
- [27] Y. Zhang, J. Zeng, R. Yuan, W. Liu, Q. Li, and L. Wu. Efficient parallel solver for rarefied gas flow using gsis. *Computers & Fluids*, 281:106374, 2023.
- [28] VA Rykov. A model kinetic equation for a gas with rotational degrees of freedom. *Fluid Dynamics*, 10(6):959–966, 1975.
- [29] Lei Wu, Craig White, Thomas J Scanlon, Jason M Reese, and Yonghao Zhang. A kinetic model of the boltzmann equation for non-vibrating polyatomic gases. *Journal of Fluid Mechanics*, 763:24–50, 2015.
- [30] Qi Li, Jianan Zeng, Wei Su, and Lei Wu. Uncertainty quantification in rarefied dynamics of molecular gas: rate effect of thermal relaxation. *Journal of Fluid Mechanics*, 917:A58, 2021.
- [31] M. D. McKay, R. J. Beckman, and W. J. Conover. A comparison of three methods for selecting values of input variables in the analysis of output from a computer code. *Technometrics*, 21(2):239–245, 1979.
- [32] Javier González, Zhenwen Dai, Philipp Hennig, and Neil D. Lawrence. Batch bayesian optimization via local penalization. In *Proceedings of the 19th International Conference on Artificial Intelligence and Statistics (AISTATS)*, volume 51 of *JMLR Workshop and Conference Proceedings*, pages 648–657, 2016.
- [33] David Eriksson, Michael Pearce, Jacob R. Gardner, Ryan D. Turner, and Matthias Poloczek. Scalable global optimization via local bayesian optimization. In *Advances in Neural Information Processing Systems*, volume 32, 2019.
- [34] Ruifeng Yuan and Lei Wu. Adjoint shape optimization from the continuum to free-molecular gas flows. *Journal of Computational Physics*, page 114102, 2025.